

Inhibition mechanism of the chloride channel TMEM16A by the pore blocker 1PBC

Raimund Dutzler (✉ dutzler@bioc.uzh.ch)

University of Zurich <https://orcid.org/0000-0002-2193-6129>

Andy Lam

University of Zurich <https://orcid.org/0000-0002-2983-3044>

Sonja Rutz

University of Zurich <https://orcid.org/0000-0003-1139-1396>

Article

Keywords:

Posted Date: March 16th, 2022

DOI: <https://doi.org/10.21203/rs.3.rs-1002931/v1>

License: © ⓘ This work is licensed under a Creative Commons Attribution 4.0 International License.

[Read Full License](#)

9 TMEM16A, a calcium-activated chloride channel involved in multiple cellular processes, is a
10 proposed target for diseases such as hypertension, asthma, and cystic fibrosis. Despite these
11 therapeutic promises, its pharmacology remains poorly understood. Here, we present a cryo-
12 EM structure of TMEM16A in complex with the channel blocker 1PBC and a detailed
13 functional analysis of its inhibition mechanism. A pocket located external to the neck region of
14 the hourglass-shaped pore is responsible for open-channel block by 1PBC and presumably also
15 by its structural analogs. The binding of the blocker stabilizes an open-like conformation of the
16 channel that involves a rearrangement of several pore helices. The expansion of the outer pore
17 enhances blocker sensitivity and enables 1PBC to bind at a site within the transmembrane
18 electric field. Our results define the mechanism of inhibition and gating and will facilitate the
19 design of new, potent TMEM16A modulators.

20 The calcium-activated chloride channel TMEM16A is a member of a eukaryotic family of
21 membrane proteins that encompasses ion channels and lipid scramblases¹⁻⁸. The protein is
22 broadly expressed and mediates vital physiological functions including fluid secretion, smooth
23 muscle contraction, and the control of electrical signaling in certain neurons⁹⁻¹². Dysfunction of
24 TMEM16A has been implicated in a number of diseases such as hypercontractility in asthmatic
25 airways and hypertensive blood vessels^{13,14}, while enhancing TMEM16A activity may improve
26 epithelial function in cystic fibrosis and other mucoobstructive diseases¹⁵⁻¹⁸. Drugs that inhibit
27 TMEM16A and its paralogs have also been shown to block SARS-CoV2 spike-induced
28 syncytia observed in the lungs of patients with COVID-19 (ref. ¹⁹). These findings suggest a
29 potential positive impact of TMEM16A modulation in the management of the pathogenesis and
30 symptoms in these diseases.

31 TMEM16A is a homodimer with each subunit containing an ion conduction pore^{20,21}. Both
32 pores act independently and are activated by the binding of two Ca²⁺ ions from the cytoplasm
33 to a conserved site situated in the proximity of the ion conduction path²²⁻²⁴. The transmembrane
34 location of the Ca²⁺ binding sites confer voltage sensitivity to the binding step²², while channel
35 gating is essentially voltage-independent when the binding sites are fully occupied^{23,25,26}. The
36 proximity of the bound Ca²⁺ ions to the pore allows the control of anion access by the agonist,
37 which dynamically shapes the electrostatic potential of the ion conduction path²⁵. During
38 activation, Ca²⁺ binding to the resting state triggers a conformational rearrangement of a pore-
39 lining helix ($\alpha 6$), which contributes to the coordination of the bound divalent cations²². This

40 movement is in turn coupled to the release of a hydrophobic gate and presumably additional
41 structural rearrangements in the narrow region of the hourglass-shaped pore, which together
42 facilitate ion conduction^{27,28}. The activation process is further modulated by an extra Ca^{2+}
43 binding site located near the dimer interface²⁹ that has been observed in the structures of the
44 mammalian scramblases TMEM16K³⁰ and F³¹. Channel activity in TMEM16 proteins, while
45 directly triggered by the binding of Ca^{2+} , is also dependent on the membrane lipid PI(4,5)P₂
46 (ref. ³²⁻³⁷), which likely regulates activation of these proteins during signaling.

47 By now, numerous TMEM16A modulators, such as E_{act} ³⁸, CaCCinh-01³⁹, T16Ainh-A01⁴⁰,
48 MONNA⁴¹, Ani9⁴², ETX001⁴³, 1PBC⁴⁴, and benzbromarone¹³, have been discovered, although
49 the precise action of most of these molecules has remained unclear^{45,46}. Several compounds
50 have been proposed to bind to the flexible loop region near the extracellular entrance of the
51 pore based on computational docking and molecular dynamics simulations^{47,48}. Other anion
52 channel blockers, such as 9-anthracene carboxylate (9-AC) and 4,4'-Diisothiocyanato-2,2'-
53 stilbenedisulfonic acid (DIDS), and the anthelmintic drug niclosamide have also been shown
54 to inhibit TMEM16A⁴⁹⁻⁵¹. Some of these molecules, including 1PBC, consist of aromatic rings,
55 and as weak acids, they are likely to interact with the anion-selective pore. However, the
56 location of their binding sites and the channel conformations to which these compounds bind
57 are not known, limiting our ability to design more potent and specific drugs that target
58 TMEM16 proteins.

59 Here, we present a cryo-EM structure of TMEM16A in complex with the inhibitor 1PBC, which
60 is selective for anion channels of the TMEM16 family, complemented by a detailed functional
61 analysis of inhibition. Together, our data reveal the molecular mechanisms underlying channel
62 blockade and gating and provide a structural basis for the future development of TMEM16A
63 modulators.

64

65 **Functional analysis of a TMEM16A blocker**

66 Given the proposed therapeutic importance of TMEM16 inhibition, we have set out to
67 understand the action of inhibitory compounds on the channel TMEM16A, whose structural
68 and functional properties have been very well characterized. To this end, we have focused on
69 the TMEM16A blocker 1PBC⁴⁴ and characterized its mechanism of action in excised inside-
70 out patches (Fig. 1). 1PBC contains two proton-accepting groups that titrate with acidic and
71 basic pKa's as predicted based on theoretical considerations⁵² (Fig. 1a). When applied from the
72 intracellular side, 1PBC blocks TMEM16A completely with an IC₅₀ of ~4 μM at zero mV and
73 saturating Ca²⁺ concentration (2 μM) (Fig. 1b, c). The potency of block increases upon
74 depolarization (Fig. 1c, d), suggesting that the compound acts on the channel from the
75 extracellular side. Since the pore would be too narrow to permit its passage²², our results imply
76 that, at neutral pH, the predominantly uncharged 1PBC is freely membrane-permeable, but that
77 it binds to the channel in a deprotonated state within the transmembrane electric field,
78 conferring the bulk of the observed voltage dependence. A closer examination of this voltage

79 dependence reveals a non-monotonic exponential variation of the IC_{50} 's (Fig. 1d), suggesting
80 that additional factors contribute to 1PBC block, potentially originating from interactions with
81 permeating anions or a change in the pore conformation. 1PBC appears to be selective for
82 TMEM16 channels, as it also blocks the channel TMEM16B, while it is ineffective in inhibiting
83 the current mediated by the scramblase TMEM16F within the same concentration range (Fig.
84 1e, f and Supplementary Fig. 1a, b), despite the considerable sequence conservation that is
85 pronounced at the extracellular part of the pore (Fig. 1g).

86 Several functional observations suggest that 1PBC predominantly acts on the open state of the
87 channel. As expected from such mechanism, the potency of block increases with open
88 probability (Fig. 2a, b). Correspondingly, elevated Ca^{2+} concentrations slow unblocking and
89 promote steady-state blockade in concentration-jump experiments (Supplementary Fig. 2a, b).

90 We modelled the Ca^{2+} dependence of 1PBC inhibition by adding a blocking step to the open
91 state in a gating mechanism that we described previously²⁸ (see 'Methods'), and fitted the
92 concentration dependence of block at +80 and -80 mV (Fig. 2a, b). Within this voltage range,
93 1PBC binds with an apparent valence of ~ 0.27 and a K_d of $\sim 3.6 \mu M$ at zero mV. The agreement
94 between the model and the data confirms that the Ca^{2+} dependence of block is due to a
95 difference in open probability (Fig. 2a, b and Supplementary Fig. 2c-e). In contrast, a closed-
96 state antagonism model predicts that increasing Ca^{2+} concentrations would antagonize
97 inhibition by 1PBC, likely due to the depletion of closed states (Supplementary Fig. 2f-h),
98 further consolidating an open-channel block mechanism and suggesting that the blocker

99 stabilizes the open state. The latter is also reflected in mutants showing pronounced basal
100 activity (as in the case of the previously characterized mutants I551A²⁷ and Q649A^{25,53}), where
101 the potency of block is decreased by about ten-fold in the ligand-free form compared to the
102 Ca²⁺-bound state (Fig. 2c and Supplementary Fig. 1c). Together, these results suggest a Ca²⁺-
103 induced conformational rearrangement at the site of inhibition.

104

105 **Structural basis of inhibition**

106 To understand the molecular interactions underlying channel block and open state stabilization,
107 we determined a cryo-EM structure of mouse TMEM16A in complex with 1PBC in the
108 presence of Ca²⁺ (Fig. 3a, b and Supplementary Figs. 3, 4). The structure was obtained by
109 combining datasets collected from samples applied to cryo-EM grids with distinct chemical
110 properties. The complementary orientations of protein particles in the two datasets allowed the
111 reconstruction of a 3D map of exceptionally high quality. With an overall resolution of 2.85 Å,
112 the final map shows well-defined density for the entire protein, including two Ca²⁺ ions bound
113 at the canonical transmembrane site and at an additional site near the dimer interface that was
114 originally identified in the structures of TMEM16K³⁰ and F³¹ and whose involvement in
115 channel activation has recently been demonstrated in TMEM16A²⁹ (Supplementary Fig. 4b, c).
116 Unlike in a previous dataset obtained in the presence of Ca²⁺, where considerable
117 conformational heterogeneity of α -helix 3 is observed²², this region is now well-resolved. The
118 improved density permitted the remodeling of the helix, which brings residues of α 3 in contact

119 with the bound blocker that would have been distant in the original conformation
120 (Supplementary Fig. 5). Notably, this $\alpha 3$ conformation (up to Arg 515 in TMEM16A) now
121 closely resembles the structure of the equivalent helix in the paralog TMEM16F³¹.

122 Non-protein density, which is not present in any of the previous maps of TMEM16A, is found
123 at the extracellular end of the hourglass-shaped pore of each subunit (Fig. 3b-d and
124 Supplementary Fig. 4d). This density is located at a site surrounded by the outer pore helices
125 $\alpha 3$ -6 and has the size and shape that can be accounted for by the structure of 1PBC (Fig. 3c, d).
126 The location of the site within the transmembrane electric field, with a fractional voltage drop
127 of ~ 0.2 as estimated from Poisson-Boltzmann calculations (Fig. 3e), is consistent with the
128 voltage dependence and the perceived mechanism of block obtained from functional
129 experiments (Fig. 1).

130 The binding site is complementary to the blocker in both its shape and polarity (Fig. 4a, b).
131 While the composition of the surrounding residues renders the pocket amphiphilic, with
132 aliphatic sidechains contacting the aromatic rings of the bound 1PBC and being enriched near
133 the entrance of the narrow pore, the positive electrostatic potential in its interior facilitates anion
134 conduction and potentially also influences the protonation state of titratable groups of the
135 blocker (Fig. 4b, c). Many of the interacting residues with hydrophobic character, including Val
136 511 and Ile 512 on $\alpha 3$, Val 543 on $\alpha 4$, Val 599 on $\alpha 5$, and Ile 636 and Ile 640 on $\alpha 6$, are within
137 van der Waals' distance from the bound 1PBC molecule (Fig. 5a, b). Mutating these residues
138 to alanine severely lowers the potency of block, with I512A, V543A, V599A, and I640A

139 exerting the most pronounced effects (Fig. 5c, d and Supplementary Figs. 6-8). In contrast, the
140 surrounding non-charged polar residues (*i.e.* Thr 539, Asn 546, and Gln 637) have less or even
141 an opposite energetic contribution, except for Thr 539, which engages in an interaction with the
142 trifluoromethyl group of 1PBC (Fig. 5a-d).

143 A putative salt bridge is observed between Lys 603 on $\alpha 5$ and the presumably deprotonated
144 1PBC hydroxyl group, which would be stabilized in the positive electrostatic environment (Fig.
145 5a, b). Mutating Lys 603 to the neutral glutamine severely lowers the potency of block by about
146 100-fold (Fig. 5c, d). Interaction with 1PBC is additionally stabilized by the closely apposed
147 Arg 515 on $\alpha 3$, which covers the blocker from the extracellular side by stacking its guanidinium
148 group over the blocker's aromatic ring and whose contribution is reflected in a profound
149 decrease in the potency of block when replaced by an alanine (Fig. 5a-d). Both positive charges
150 also appear to be essential to the voltage dependence of block, as 1PBC fails to inhibit with a
151 higher affinity in the investigated voltage range (Fig. 5c and Supplementary Figs. 6-8). In
152 contrast, the truncation of the Arg 535 sidechain on $\alpha 4$ that is located further away from the
153 binding site exerts a smaller effect which might result from long-range Coulombic interactions
154 (Fig. 5a-d).

155

156 **Conformational rearrangement of the outer pore**

157 In addition to the inhibition mechanism, the structure of the blocked channel provides detailed
158 insight into the conformational changes in the extracellular part of the pore upon activation that,

159 due to the blurred density of $\alpha 3$, have remained unresolved in the Ca^{2+} -bound and -free states
160 of the wild-type protein (WT)²². Whereas the here obtained structure defines the extracellular
161 pore in a Ca^{2+} -bound open conformation with $\alpha 3$ adopting an ‘up’ position, the previously
162 determined structure of the TMEM16A mutant I551A in the absence of Ca^{2+} displays a ‘down’
163 conformation of the same helix in the Ca^{2+} -free state²⁷ (Supplementary Fig. 5a, b). Although of
164 lower quality, the ensemble of the ‘up’ and ‘down’ conformations largely match the density in
165 both the Ca^{2+} -free and Ca^{2+} -bound states of WT, accounting for the apparent structural
166 heterogeneity in the corresponding maps (Supplementary Fig. 5c, d).

167 With respect to its overall conformation, the features of TMEM16A in complex with 1PBC
168 closely resemble the previously determined Ca^{2+} -bound structure of the channel, although the
169 binding of 1PBC leads to a rearrangement of a pocket that is also sampled in the unblocked
170 state (Fig. 6a and Supplementary Fig. 5d). In contrast, the comparison to the Ca^{2+} -free apo
171 protein and the constitutively active mutant I551A obtained under equivalent conditions shows
172 a pronounced change in the orientation and flexibility of α -helices 3, 4, and 6, all lining the pore
173 and being involved in gating-related conformational rearrangements (Fig. 6a). Besides the
174 previously described change in $\alpha 6$ (ref. ²²), the present structure reveals the differences in $\alpha 3$
175 and $\alpha 4$ between Ca^{2+} -free and -bound states that likely underlie the activation of the
176 extracellular part of the pore (Fig. 6b). These differences include an outward movement of the
177 N-terminal part of $\alpha 4$ by about 6° resulting in the displacement of $\text{C}\alpha$ positions of up to 3 Å,
178 leading to a widening of the entrance of the inhibitor binding pocket (Fig. 6c). A much more

179 extended transition is found in $\alpha 3$, where the rearrangement of the helix changes its tilt and
180 results in a clockwise rotation of about 60° around its axis and an upward shift of about 6 Å
181 from the Ca^{2+} -free to the Ca^{2+} -bound state (Fig. 6b, c). The described conformational change
182 relocates Tyr 514, which occupies the 1PBC binding site in the Ca^{2+} -free state, away from the
183 pore region and brings Arg 515 in contact with the blocker (Fig. 6c, d and Supplementary Fig.
184 4d). This transition thus shapes a binding pocket that is essentially not present in the Ca^{2+} -free
185 state, explaining the low affinity of the blocker in the closed conformation of the channel (Fig.
186 6e).

187 The described rearrangement is also consistent with the effect of mutations on 1PBC binding.
188 Whereas residues of $\alpha 3$ found in vicinity of the blocker in the ‘up’ conformation observed in
189 the blocked structure exert a strong influence on inhibitor potency, residues that would
190 otherwise make contact with the blocker in the ‘down’ conformation have a minimal effect
191 (Fig. 5d). Although not having any net energetic effect on activation²⁷, the comparatively large
192 impact of truncating the Tyr 514 sidechain on blocker binding (Fig. 5d), which has moved out
193 of the binding site to interact with $\alpha 4$ (Fig. 6c, d), reflects the importance of this residue in
194 stabilizing the observed channel conformation. Collectively, the described conformational
195 changes result in major rearrangements of residues on $\alpha 3$, including the positively charged Arg
196 515 and the hydrophobic Val 508, Val 511, and Ile 512 that are all in contact with the bound
197 blocker, and a comparatively smaller repositioning of pore-lining residues on $\alpha 4$ and 6,
198 including Val 543, Asn 546, and Ile 551 that have partially retracted from the pore lumen (Fig.

199 7a). In this state, the outer pore and the neck region both have a dimension sufficient to
200 accommodate a Cl⁻ or even the larger I⁻ ion, while the inner gate region remains partially
201 constricted, with a diameter that might be still too narrow to be sterically conductive (Fig. 6e
202 and Fig. 7b, c).

203 The described movements of the pore-lining helices appear to be facilitated by glycine residues
204 located on the three helices involved in the conformational changes. These include the
205 conserved Gly 510 on α 3 located in vicinity of the inhibitor binding site, Gly 558 on α 4 situated
206 at the intracellular vestibule, and the previously characterized Gly 644 on α 6 that serves as a
207 hinge for the rearrangement of the helix upon Ca²⁺ binding²² (Fig. 8a). Replacing Gly 558 with
208 the more rigid proline exerts appreciable effects on anion conduction and Ca²⁺ potency (Fig.
209 8a-d), which correspond to a moderate increase in the barriers for permeation and a stabilization
210 of the closed state of the channel. The same mutation did not interfere with block by 1PBC (Fig.
211 8e), which might be expected for a residue that is remote from the site of inhibition and whose
212 conformation was not observed to undergo large rearrangements (Fig. 8a). In contrast, the
213 equivalent mutation of Gly 510 has a more pronounced effect on ion conduction, as manifested
214 in the strong outward rectification of current reflecting the elevation of energy barriers caused
215 by the obstruction of the pore (Fig. 8a-c). As for G558P, the decrease in the potency of Ca²⁺
216 results from the stabilization of the closed state (Fig. 8d). However, different from the glycine
217 on α 4, the concurrent large effect of mutating Gly 510 on the potency of block and the loss of

218 its voltage dependence further emphasize the importance of conformational changes in $\alpha 3$ for
219 pore opening and inhibition (Fig. 8e).

220

221 **Mechanism**

222 Our study addressing the inhibition of TMEM16A provides a detailed mechanism of open-
223 channel block and permits insight into the gating transitions at the extracellular part of the pore.

224 In the Ca^{2+} -free closed state of the channel, the pore remains constricted throughout and is
225 sterically unfavorable for the access of either anions or the blocker 1PBC, whose binding site
226 has collapsed and is occupied by a residue on $\alpha 3$ (Tyr 514). Upon Ca^{2+} binding, the channel
227 progressively transitions towards a conducting state by rearranging the outer vestibule, which
228 creates a site that accommodates the blocker (Fig. 9). The enhanced occupancy of the open state
229 increases the availability of this site, explaining how elevated Ca^{2+} concentrations promote
230 channel blockade (Fig. 2, Supplementary Fig. 2, and ref. ⁴⁴). The Ca^{2+} -dependent remodeling
231 of the outer pore is also reflected in the lower potency of the blocker in the absence of Ca^{2+} in
232 the constitutively active mutants observed here (Fig. 2c) and in a related study reporting the
233 inhibition by the compound 9-AC, whose binding site was proposed to be located further
234 towards the cytoplasm⁵⁴. In contrast, the predicted location of inhibitors based on docking
235 studies would be extracellular to the described site of 1PBC^{47,48}.

236 In the open state, 1PBC accesses the pore from the extracellular side and binds at the border to
237 the narrow neck region of the hourglass-shaped pore, thereby impeding ion conduction (Fig. 3).

238 Access from the cytoplasm, in contrast, is prohibited by the narrow diameter of the neck, which
239 precludes the diffusion of even smaller solutes²². The binding of 1PBC is promoted by both
240 steric and chemical complementarity, with several positively charged residues stabilizing the
241 blocker in its binding site (Figs. 4, 5), consistent with a previous investigation⁴⁴. Given the
242 specific interactions between the channel and 1PBC, different mechanisms might account for
243 the reported inhibition of TMEM16A by structurally unrelated compounds. As a weak acid, the
244 transfer of 1PBC from an aqueous to a protein environment is likely accompanied by a shift in
245 its pKa. Although mostly uncharged in solution, the interaction with Lys 603 and the positive
246 electrostatic environment of the binding site stabilize the bound inhibitor in its deprotonated
247 form, thus increasing its binding affinity. The ensuing ionization of 1PBC and the release of the
248 dissociated proton act as a source for the observed voltage dependence of block. Neutralizing
249 Lys 603 abolishes these mechanisms, thereby resulting in a complete loss of voltage sensitivity
250 within the investigated voltage range (Fig. 5 and Supplementary Figs. 6-8).

251 The binding of 1PBC stabilizes several structural changes involved in channel gating.
252 Following the rearrangement of $\alpha 6$ that accompanies Ca^{2+} binding, $\alpha 3$ and to a lesser extent the
253 extracellular parts of $\alpha 4$ undergo conformational changes that together lead to an expansion of
254 the outer pore and the neck region (Figs. 6, 7). These transitions are mediated by three glycine
255 residues, one on each transmembrane segment, which presumably enable the helices to bend
256 away from the pore lumen as the channel opens (Fig. 8). While flexibility in the hinge region
257 of $\alpha 6$ allows its relaxation to the resting state upon the dissociation of the bound Ca^{2+} (ref. ²²),

258 the flexibility of equivalent residues on $\alpha 3$ and $\alpha 4$ facilitates the rearrangement of these helices
259 during pore opening. These structural changes are reminiscent of an outer-pore gate that was
260 proposed to open upon Ca^{2+} binding during activation, providing access to the inhibitor 9-AC⁵⁴.
261 Glycine-mediated conformational changes constitute a general mechanism underlying the
262 gating of channel proteins and have also been observed in certain potassium channels, where
263 they facilitate the expansion of an otherwise inaccessible inner vestibule⁵⁵. The ability of $\alpha 3$ to
264 alter its conformation during gating, which on its extracellular side effects the pore geometry
265 and on its intracellular side alters the environment of a putative PI(4,5)P₂ binding site³³, hints
266 at a potential role of this helix during PI(4,5)P₂ regulation of the channel. In the 1PBC-bound
267 structure, the dilation of the outer part of the pore appears to be sufficient to accommodate
268 permeating ions, whereas the inner gate region might still be too narrow to be fully conductive
269 (Fig. 7c). Both features suggest that the expansion of the outer pore would precede the widening
270 of the narrow constriction during the transition into a conducting state and that the presented
271 structure might be stabilized in a partially open conformation. This is consistent with a
272 postulated mechanism of channel activation where successive transitions are required for the
273 release of a hydrophobic gate located on the intracellular end of the narrow pore as a final step
274 in the gating process^{27,28}.

275 In summary, our study has provided comprehensive insights into the mechanism of
276 antagonizing channel activity in TMEM16A. A binding pocket located immediately external to
277 the neck region of the hourglass-shaped pore is responsible for open-channel block by 1PBC

278 and presumably structurally related compounds. The binding of Ca^{2+} and the blocker shifts the
279 conformational equilibrium towards the open state in a process that involves the movement of
280 several pore helices, which, although pronounced, are less extensive than observed in fungal
281 family members functioning as lipid scramblases^{56,57}. Despite the conservation of residues
282 forming the extracellular vestibule, 1PBC is selective for anion channels of the TMEM16
283 family over the scramblase TMEM16F, a feature that is also reported for the Cl^- channel
284 inhibitors NFA and NPPB⁵. In the case of 1PBC, this is likely a consequence of conformational
285 differences in the region surrounding the binding site, reflecting the distinct functional
286 properties of these paralogs. The structure of TMEM16A in a blocker-bound, partially open
287 state presented here may thus lead to the rational design of specific small molecules for its
288 therapeutic targeting in conditions such as hypertension, asthma, and cystic fibrosis.

289

290 **Methods**

291 **Molecular biology and cell culture**

292 HEK293T cells (ATCC CRL-1573) were maintained in Dulbecco's modified Eagle's medium
293 (DMEM; Sigma-Aldrich) supplemented with 10 U ml^{-1} penicillin, 0.1 mg ml^{-1} streptomycin
294 (Sigma-Aldrich), 2 mM L-glutamine (Sigma-Aldrich), and 10% FBS (Sigma-Aldrich) in a
295 humidified atmosphere containing 5% CO_2 at $37 \text{ }^\circ\text{C}$. HEK293S GnTI⁻ cells (ATCC CRL-3022)
296 were maintained in HyClone HyCell TransFx-H medium (GE Healthcare) supplemented with
297 10 U ml^{-1} penicillin, 0.1 mg ml^{-1} streptomycin, 4 mM L-glutamine, 0.15% poloxamer 188

298 (Sigma-Aldrich), and 1% FBS in an atmosphere containing 5% CO₂ at 185 rpm at 37 °C. The
299 *ac* splice variant of mouse TMEM16A (UniProt ID: Q8BHY3), mouse TMEM16B (UniProtID:
300 Q8CFW1), or mouse TMEM16F (UniProt ID: Q6P9J9) bearing a 3C cleavage site, a Venus
301 YFP, a Myc tag, and a Streptavidin-binding peptide (SBP) downstream of the open reading
302 frame in a modified pcDNA3.1 vector (Invitrogen) were used as described previously^{21,31}.
303 Mutations were introduced using a modified QuikChange method⁵⁸ and were verified by
304 sequencing.

305

306 **Protein expression and purification**

307 GnT1⁻ cells were transiently transfected with wild-type mouse TMEM16A complexed with
308 Polyethylenimine MAX 40 K (formed in non-supplemented DMEM medium at a w/w ratio of
309 1:2.5 for 30 minutes). Immediately after transfection, the culture was supplemented with 3.5
310 mM valproic acid. Cells were collected 48 h post-transfection, washed with PBS, and stored at
311 -80 °C until further use. Protein purification was carried out at 4 °C and was completed within
312 12 hours. The protein was purified in Ca²⁺-free buffers and was supplemented with 1 mM free
313 Ca²⁺ when indicated during cryo-EM sample preparation. Cells were resuspended and
314 solubilized in 150 mM NaCl, 5 mM EGTA, 20 mM HEPES, 1x cOmplete protease inhibitors
315 (Roche), 40 µg ml⁻¹ DNase (AppliChem), 2% GDN (Anatrace) at pH 7.4 by gentle mixing for
316 2 hours. The solubilized fraction was obtained by centrifugation at 16,000 g for 30 minutes.
317 After filtration with 0.5 µm filters (Sartorius), the supernatant was incubated with streptavidin

318 UltraLink resin (Pierce, Thermo Fisher Scientific) for 2 hours under gentle agitation. The beads
319 were loaded onto a gravity column and were washed with 60 column volume of SEC buffer
320 containing 150 mM NaCl, 2 mM EGTA, 20 mM HEPES, 0.01% GDN at pH 7.4. The bound
321 protein was eluted by incubating the beads with 3 column volumes of SEC buffer supplemented
322 with 0.25 mg ml⁻¹ 3C protease for 30 minutes. The eluate was concentrated using a 100 kDa
323 cutoff filter, filtered through a 0.22 µm filter, and loaded onto a Superose 6 10/300 GL column
324 (GE Healthcare) pre-equilibrated with SEC buffer. Peak fractions containing the protein were
325 pooled, concentrated, and used immediately for cryo-EM sample preparation.

326

327 **Cryo-EM sample preparation and data collection**

328 2.5 µl of purified protein, concentrated to ~1.5 mg ml⁻¹ and pre-incubated with 100 µM 1PBC
329 and 1 mM free Ca²⁺ for at least 30 minutes at 4 °C, was applied onto holey carbon grids
330 (Quantifoil Au R1.2/1.3, 300 mesh). Immediately prior to sample application, grids were glow-
331 discharged at 15 mA for 30 seconds. After sample application, grids were blotted for 1–3
332 seconds with a blot force setting of 0 at 4 °C at 100% humidity, plunge-frozen in a liquid
333 propane/ethane mixture using Vitrobot Mark IV (Thermo Fisher Scientific) and stored in liquid
334 nitrogen until further use. To alleviate preferred orientation of the protein particles, samples
335 were also vitrified on holey carbon grids pre-deposited with graphene oxide (GO) (Sigma-
336 Aldrich), prepared as described⁵⁹. In this case, the purified protein was used at ~0.7 mg ml⁻¹

337 and pre-incubated with the same concentration of 1PBC and Ca^{2+} , and the grids were not glow-
338 discharged prior to sample application.

339 Data collection was performed on a 300 kV Titan Krios G3i (Thermo Fisher Scientific)
340 equipped with a post-column quantum energy filter (20 eV slit width) and a K3 summit direct
341 electron detector (Gatan) in super-resolution mode. Dose-fractionated micrographs were
342 collected at a nominal magnification of 130,000x corresponding to a pixel size of 0.651 Å pixel⁻¹
343 (0.326 Å pixel⁻¹ in super-resolution) and a nominal defocus range of -1 to -2.4 μm using EPU
344 2.9 (Thermo Fisher Scientific). Each movie contained 36 frames with a total exposure time of
345 1.01 s and a total dose of approximately 61 e⁻ Å⁻² (1.696 e⁻ Å⁻² frame⁻¹) or approximately 70 e⁻
346 Å⁻² (1.937 e⁻ Å⁻² frame⁻¹) for the datasets obtained from non-coated and graphene oxide-coated
347 grids respectively.

348

349 **Cryo-EM data processing**

350 The datasets were processed in RELION 3.1 (ref. ⁶⁰). Micrographs were binned 3x (0.9765 Å
351 pixel⁻¹) and were preprocessed using RELION's own implementation of MotionCor2 (ref. ⁶¹)
352 and Gctf⁶². crYOLO⁶³ was used for automated particle picking, resulting in 2,203,806 and
353 1,596,293 respectively for the normal and GO datasets (6,719 and 13,416 movies respectively).
354 Particles were extracted with a box size of 360 pixels with 2x binning (180-pixel box, 1.95 Å
355 pixel⁻¹) and were subjected to two rounds of 2D classification, separately for each dataset.
356 Selected classes were pooled, resulting in 387,552 particles (197,894 and 189,658 from the
357 normal and GO datasets respectively), and were 3D-classified without symmetry applied using

358 a previous Ca²⁺-bound TMEM16A map low-pass filtered to 20 Å as a reference. Particles from
359 the most isotropic class (101,813 particles, 13,897 and 87,916 from the normal and GO datasets
360 respectively) were re-extracted with a box size of 400 pixels unbinned (0.9765 Å pixel⁻¹) and
361 were refined with C2 symmetry applied, resulting in a 3.39 Å map. A final map of 2.85 Å was
362 obtained after several rounds of CTF refinement and Bayesian polishing, and a masked
363 refinement excluding the detergent micelle upon convergence in the final refinement. Global
364 and directional Fourier shell correlations (FSCs) between the half-maps were estimated using
365 the 3DFSC server (<https://3dfsc.salk.edu/>)⁶⁴.

366

367 **Model building and refinement**

368 The initial model was obtained by fitting a previously determined Ca²⁺-bound TMEM16A
369 structure²⁷ (PDB: 7B5C) into the density of the Ca²⁺/1PBC-bound TMEM16A using Chimera⁶⁵.
370 The coordinates and geometry restraints for the ligand 1PBC were generated using eLBOW⁶⁶.
371 The combined model was iteratively rebuilt in Coot⁶⁷ and refined in Phenix⁶⁸ with ligand
372 geometry restraints applied. The geometry of the final models was evaluated using
373 MolProbity⁶⁹. Potential overfitting was evaluated by comparing FSC_{work} and FSC_{free}. Pore radii
374 were calculated using HOLE⁷⁰. Figures containing molecular structures and maps were
375 prepared using VMD⁷¹ and ChimeraX⁷².

376

377 **Electrophysiology**

378 HEK293T cells were transfected with 3–4 μg DNA per 6 cm Petri dish using the calcium
379 phosphate co-precipitation method and were used within 24–96 h after transfection. Recordings
380 were performed on inside-out patches excised from HEK293T cells expressing the construct of
381 interest. Patch pipettes were pulled from borosilicate glass capillaries (O.D. 1.5 mm, I.D. 0.86
382 mm, Sutter Instrument) and were fire-polished with a microforge (Narishige) before use. Pipette
383 resistance was typically 3–8 $\text{M}\Omega$ when filled with the recording solutions detailed below. Seal
384 resistance was typically 4 $\text{G}\Omega$ or higher. Voltage-clamp recordings were made using Axopatch
385 200B, Digidata 1550, and Clampex 10.7 (Molecular Devices). Analog signals were filtered with
386 the in-built 4-pole Bessel filter at 10 kHz and were digitized at 20 kHz. Solution exchange was
387 achieved using a gravity-fed system through a theta glass pipette mounted on an ultra-fast piezo-
388 driven stepper (Siskiyou). Liquid junction potential was found to be consistently negligible
389 given the ionic composition of the solutions and was therefore not corrected. All recordings
390 were performed at 20 $^{\circ}\text{C}$.

391 A symmetrical ionic condition was used throughout. Stock solution with Ca^{2+} -EGTA contained
392 150 mM NaCl, 5.99 mM $\text{Ca}(\text{OH})_2$, 5 mM EGTA, and 10 mM HEPES at pH 7.40. Stock solution
393 with EGTA contained 150 mM NaCl, 5 mM EGTA, and 10 mM HEPES at pH 7.40. Free Ca^{2+}
394 concentrations were adjusted by mixing the stock solutions at the required ratios calculated
395 using the WEBMAXC program (<http://web.stanford.edu/~cpatton/webmaxcS.htm>). Patch
396 pipettes were filled with the stock solution with Ca^{2+} -EGTA, which has a free Ca^{2+}
397 concentration of 1 mM. 1PBC (ChemBridge) stock was reconstituted in anhydrous DMSO

398 (Sigma-Aldrich) at 100 mM and stored at -20 °C. Working solutions with 1PBC were prepared
 399 by serial dilution. Unless otherwise stated, experiments were performed at a saturating Ca²⁺
 400 concentration as shown in Supplementary Table 1 and the primary data were corrected for
 401 current rundown as described previously^{21,25}.

402

403 **Data analysis**

404 Concentration-response relations, obtained from the ratio of the I-V plots before and after the
 405 application of the blocker, were fitted to the Hill equation,

$$I/I_{max} = \frac{1}{1 + \left(\frac{IC_{50}}{[blocker]}\right)^h} \quad (1)$$

406 where I/I_{max} is the normalized current responses, IC_{50} defines the concentration at which
 407 inhibition is at its half-maximum, and h is the Hill coefficient.

408 I-V data were fitted to a minimal permeation model that accounts for the fundamental
 409 biophysical behavior of mTMEM16A as described previously²³,

$$I = zFAe^{\frac{zFV}{2nRT}} \frac{c_i - c_o e^{\frac{zFV}{RT}}}{e^{-zFV\frac{n-1}{nRT}} + \left(\frac{1}{\sigma_h}\right) \frac{1 - e^{-zFV\frac{n-2}{nRT}}}{e^{\frac{zFV}{nRT}} - 1} + \frac{1}{\sigma_\beta}} \quad (2)$$

410 where I is the current, n is the number of barriers, c_i and c_o are the intracellular and extracellular
 411 concentrations of the charge carrier, z is the valence of Cl⁻, V is the membrane voltage, and R ,
 412 T , and F have their usual thermodynamic meanings. $A = \beta_0 v$ is a proportionality factor where

413 β_0 is the value of β when $V = 0$ and v is a proportionality coefficient that has a dimension of
 414 volume. σ_h and σ_β are respectively the rate of barrier crossing at the middle and the innermost
 415 barriers relative to that at the outermost barrier (β). The best-fit values of σ_β and σ_h at zero and
 416 saturating Ca^{2+} concentrations were used to calculate $\Delta E_{a(\sigma_\beta)}$ and $\Delta E_{a(\sigma_h)}$, the difference
 417 between the activation energy at the innermost barrier and the middle barrier relative to that of
 418 the outermost respectively, using

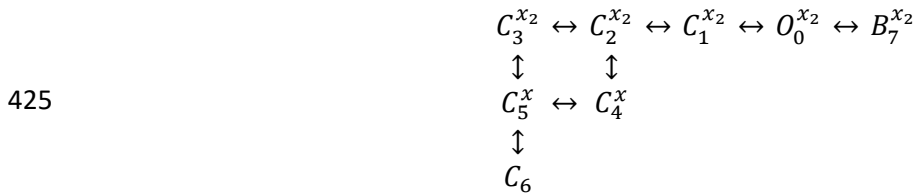
$$\Delta E_{a(\sigma_\beta)} = -RT \ln \sigma_\beta$$

$$\Delta E_{a(\sigma_h)} = -RT \ln \sigma_h$$
(3)

419

420 Mechanisms and calculations

421 The inhibition profiles of 1PBC at different Ca^{2+} concentrations were fitted to a mechanism
 422 assuming that the blocker preferentially binds to the open state. This was incorporated by
 423 adding a blocker binding step to the open state in a gating mechanism that we described
 424 previously²⁸ as follows



426 where C, O, and B correspond to the closed, open, and blocked states respectively, and the
 427 subscripts denotes the number assigned to the states. The matrix notation of this mechanism⁷³
 428 is

$$(4) \quad \mathbf{Q} = \begin{bmatrix} -k_{01} - bk_{07}v_{07}^{\delta_b/2} & k_{01} & 0 & 0 & 0 & 0 & 0 & 0 & bk_{07}v_{07}^{\delta_b/2} \\ k_{10} & -k_{10} - k_{12} & k_{12} & 0 & 0 & 0 & 0 & 0 & 0 \\ 0 & k_{21} & -k_{21} - k_{23} - k_{24} & k_{23} & k_{24} & 0 & 0 & 0 & 0 \\ 0 & 0 & k_{32} & -k_{32} - k_{35}v_{35}^{\delta_{Ca}/2} & 0 & k_{35}v_{35}^{\delta_{Ca}/2} & 0 & 0 & 0 \\ 0 & 0 & xk_{42}v_{42}^{\delta_{Ca}/2} & 0 & -xk_{42}v_{42}^{\delta_{Ca}/2} - k_{45} & k_{45} & 0 & 0 & 0 \\ 0 & 0 & 0 & xk_{53}v_{53}^{\delta_{Ca}/2} & k_{54} & -xk_{53}v_{53}^{\delta_{Ca}/2} - k_{54} - k_{56}v_{56}^{\delta_{Ca}/2} & k_{56}v_{56}^{\delta_{Ca}/2} & 0 & 0 \\ 0 & 0 & 0 & 0 & 0 & xk_{65}v_{65}^{\delta_{Ca}/2} & -xk_{65}v_{65}^{\delta_{Ca}/2} & 0 & 0 \\ k_{70}v_{70}^{\delta_b/2} & 0 & 0 & 0 & 0 & 0 & 0 & 0 & -k_{70}v_{70}^{\delta_b/2} \end{bmatrix}$$

429 where x and b are the molar concentration of Ca^{2+} and the blocker respectively, and the
 430 subscripts indicate the transition described by the rate constant k in s^{-1} , for example k_{01}
 431 corresponds to the rate constant of the transition from state 0 to 1. δ_b and δ_{Ca} are the fraction
 432 of membrane potential that modulates the corresponding transitions. The voltage (V)
 433 dependence of the rate constants is denoted v with the same subscripts, where

$$v_{07} = e^{-z_b VF/RT} \quad (5)$$

$$v_{70} = e^{z_b VF/RT}$$

434 and

$$v_{56} = v_{35} = e^{-z_{Ca} VF/RT} \quad (6)$$

$$v_{65} = v_{53} = e^{z_{Ca} VF/RT}$$

435 and z_b and z_{Ca} are the valence of the blocker and Ca^{2+} respectively.

436 The equilibrium occupancy of states was calculated using^{73,74}

$$\mathbf{P}(\infty) = \mathbf{P}(0)(\mathbf{V}_{\lambda=0}\mathbf{V}^{-1}_{\lambda=0}) \quad (7)$$

437 where $\mathbf{P}(0)$ is the initial occupancy and \mathbf{V} can be obtained from the Eigen decomposition of \mathbf{Q}

$$\mathbf{Q} = \mathbf{V}\mathbf{\Lambda}\mathbf{V}^{-1} \quad (8)$$

438 and

$$\mathbf{\Lambda} = \begin{bmatrix} \lambda_1 & & \\ & \ddots & \\ & & \lambda_n \end{bmatrix} \quad (9)$$

$$\mathbf{V} = \begin{bmatrix} v_{11} & \cdots & v_{n1} \\ \vdots & \ddots & \vdots \\ v_{1n} & \cdots & v_{nn} \end{bmatrix}$$

439 are the Eigenvalue and Eigenvector matrices respectively. The open probability calculated
 440 using Eq. 7 was used to compute the squared difference for each data point. The total sum of
 441 squares, consisting of the inhibition profiles at the indicated Ca^{2+} concentrations and the Ca^{2+}
 442 activation responses in open probability at the given membrane voltages (-80 and 80 mV), was
 443 minimized to estimate the affinity of the blocker in the open state ($K_{d\ 1PBC}$) and the fraction of
 444 the membrane potential that modulates the binding of the blocker and Ca^{2+} (δ_b and δ_{Ca}
 445 respectively).

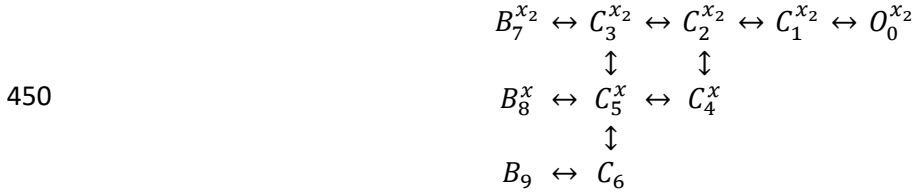
446 The time course of simulated concentration-jump experiments was calculated using^{73,74}

$$\mathbf{P}(t) = \mathbf{P}(0) \sum_{i=1}^n \mathbf{A}_i e^{\lambda_i t} \quad (10)$$

447 where $\mathbf{P}(t)$ and $\mathbf{P}(0)$ are the occupancy of states at time t and zero ($t = 0$) respectively, λ_i are
 448 the diagonal values of the Eigenvalue matrix $\mathbf{\Lambda}$, and

$$\mathbf{A}_i = \mathbf{V}_{i^{th}col} \mathbf{V}^{-1}_{i^{th}row} \quad (11)$$

449 For the closed-state antagonism model, the following scheme was used



451 The corresponding matrix notation of this mechanism is

$$\mathbf{Q} = \begin{bmatrix}
 -k_{01} & k_{01} & 0 & 0 & 0 & 0 & 0 & 0 & 0 & 0 & 0 & 0 & 0 & 0 & 0 & 0 & 0 & 0 & 0 & 0 & 0 \\
 k_{10} & -k_{10} - k_{12} & k_{12} & 0 & 0 & 0 & 0 & 0 & 0 & 0 & 0 & 0 & 0 & 0 & 0 & 0 & 0 & 0 & 0 & 0 & 0 \\
 0 & k_{21} & -k_{21} - k_{23} - k_{24} & k_{23} & k_{24} & 0 & 0 & 0 & 0 & 0 & 0 & 0 & 0 & 0 & 0 & 0 & 0 & 0 & 0 & 0 & 0 \\
 0 & 0 & k_{32} & -k_{32} - k_{35} v_{35}^{\delta_{ca}/2} - b k_{37} v_{37}^{\delta_b/2} & 0 & 0 & k_{35} v_{35}^{\delta_{ca}/2} & 0 & 0 & b k_{37} v_{37}^{\delta_b/2} & 0 & 0 & 0 & 0 & 0 & 0 & 0 & 0 & 0 & 0 & 0 \\
 0 & 0 & x k_{42} v_{42}^{\delta_{ca}/2} & 0 & 0 & -x k_{42} v_{42}^{\delta_{ca}/2} - k_{45} & k_{45} & 0 & 0 & 0 & 0 & 0 & 0 & 0 & 0 & 0 & 0 & 0 & 0 & 0 & 0 \\
 0 & 0 & 0 & x k_{53} v_{53}^{\delta_{ca}/2} & 0 & 0 & -x k_{53} v_{53}^{\delta_{ca}/2} - k_{54} - k_{56} v_{56}^{\delta_{ca}/2} - b k_{58} v_{58}^{\delta_b/2} & k_{54} v_{54}^{\delta_{ca}/2} & 0 & 0 & b k_{58} v_{58}^{\delta_b/2} & 0 & 0 & 0 & 0 & 0 & 0 & 0 & 0 & 0 & 0 \\
 0 & 0 & 0 & 0 & 0 & 0 & 0 & x k_{65} v_{65}^{\delta_{ca}/2} & 0 & 0 & 0 & 0 & 0 & 0 & 0 & 0 & 0 & 0 & 0 & 0 & 0 & 0 \\
 0 & 0 & 0 & 0 & 0 & 0 & 0 & 0 & 0 & 0 & -x k_{65} v_{65}^{\delta_{ca}/2} - b k_{69} v_{69}^{\delta_b/2} & 0 & 0 & 0 & 0 & 0 & 0 & 0 & 0 & 0 & 0 \\
 0 & 0 & 0 & k_{73} v_{73}^{\delta_b/2} & 0 & 0 & 0 & 0 & 0 & 0 & -k_{73} v_{73}^{\delta_b/2} & 0 & 0 & 0 & 0 & 0 & 0 & 0 & 0 & 0 & 0 \\
 0 & 0 & 0 & 0 & 0 & 0 & 0 & k_{85} v_{85}^{\delta_b/2} & 0 & 0 & 0 & -k_{85} v_{85}^{\delta_b/2} & 0 & 0 & 0 & 0 & 0 & 0 & 0 & 0 & 0 \\
 0 & 0 & 0 & 0 & 0 & 0 & 0 & 0 & 0 & 0 & k_{96} v_{96}^{\delta_b/2} & 0 & 0 & 0 & 0 & 0 & 0 & 0 & 0 & 0 & -k_{96} v_{96}^{\delta_b/2}
 \end{bmatrix}$$

(12)

452 where

$$v_{37} = v_{58} = v_{69} = e^{-z_b VF/RT} \quad (13)$$

$$v_{73} = v_{85} = v_{96} = e^{z_b VF/RT}$$

453

454 Calculation of the transmembrane potential

455 The fraction of transmembrane potential was calculated from the Ca^{2+} /1PBC-bound

456 TMEM16A model omitting the bound 1PBC by solving the modified Poisson-Boltzmann (PB-

457 V) equation⁷⁵ implemented in the PBEQ module⁷⁶ in CHARMM⁷⁷. The calculation was run on

458 a 240 Å x 240 Å x 260 Å grid (1 Å grid spacing) followed by focusing on a 160 Å x 160 Å x

459 160 Å grid (0.5 Å grid spacing). Hydrogen positions were generated in CHARMM. The

460 membrane boundaries and dielectric properties of the system were as described previously. A
461 dielectric of 2 was assigned to the protein. The membrane was represented as a 35 Å slab with
462 a dielectric of 2. A 5 Å slab was included on each side of the membrane to account for the
463 headgroup region and was assigned a dielectric of 30. The solvent on either side of the
464 membrane and the aqueous crevices of the pore were assigned a dielectric of 80. The
465 coordinates for which the transmembrane potential is plotted were obtained from HOLE. All
466 protein charges were turned off for the calculation of the membrane potential profile⁷⁵.

467

468 **Statistics**

469 Data analysis was performed using Clampfit 10.7 (Molecular Devices), Excel (Microsoft),
470 NumPy (<https://numpy.org>), and SciPy (<https://scipy.org>). For numerical calculations, NumPy
471 and SciPy were used. Parameter optimization was performed using the described sum of squares
472 objective functions with the least_squares function in SciPy, which also computes the Jacobian
473 matrix that was used to estimate the 95% confidence intervals. Experimental data consisting of
474 individual measurements are presented as mean ± SEM. Estimated parameters are presented as
475 best-fit ± 95% confidence interval unless otherwise stated. Standard error uncertainties of
476 estimated parameters were propagated using

$$\sigma_{(a+b \text{ or } a-b)} = \sqrt{\sigma_a^2 + \sigma_b^2} \quad (14)$$

$$\frac{\sigma_{(ab \text{ or } a/b)}}{|f(a, b)|} = \sqrt{\left(\frac{\sigma_a}{|a|}\right)^2 + \left(\frac{\sigma_b}{|b|}\right)^2}$$

477 The t-test, with a significance level of 0.05, was used for statistical comparison.

478

479 **Acknowledgements**

480 This work was supported a grant of the European Research Council (ERC no 339116, AnoBest)

481 and a Forschungskredit of the University of Zurich (grant no FK-18-048) to Andy K. M. Lam.

482 The Center for Microscopy and Image Analysis (ZMB) of the University of Zurich is

483 acknowledged for the support and access to the electron microscope. The cryo-electron

484 microscope and K3 camera were acquired with support of the Baugarten and Schwyzer-Winiker

485 foundations and a Requip grant of the Swiss National Science Foundation. We thank Monique

486 Straub, Katarzyna Drozdzyk, and Marta Sawicka for help during cryo-EM data collection. All

487 members of the Dutzler laboratory are acknowledged for their help at various stages of the

488 project.

489

490 **Author contributions**

491 A.K.M.L. conceived the study and performed research. S. R. and A.K.M.L. collected cryo-EM

492 data. A.K.M.L. and R.D. jointly wrote the manuscript.

493

494 **Competing interests**

495 The authors declare no competing interests.

496

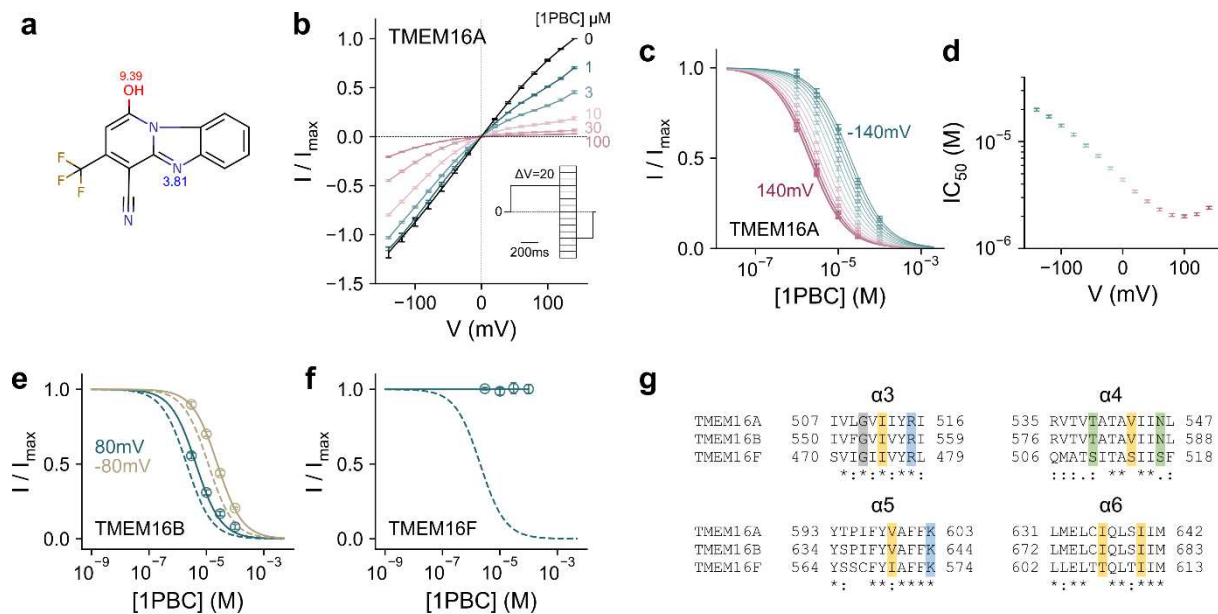
497 **Data availability**

498 Data supporting the findings of this study are available from the corresponding authors upon
499 reasonable request. The cryo-EM map, half-maps, and mask have been deposited in the Electron
500 Microscopy Data Bank under accession number EMD-xxxxx. Coordinates for the model are
501 available in the Protein Data Bank under PDB xxxx.

502

503 **Figure legends**

504



505

506 **Fig. 1: Functional characterization of the TMEM16A blocker 1PBC. a**, Chemical structure of 1PBC.

507 The pKa values of ionizable groups were calculated with the chemistry package Chemicalize

508 (ChemAxon, <https://chemicalize.com/>). **b**, Steady-state current-voltage relationship of wild-type

509 mouse TMEM16A at the indicated concentrations of 1PBC applied to the intracellular side of the

510 membrane at 2 μM intracellular Ca²⁺. Data are averages of 6 biological replicates, errors are SEM. **c**,

511 Concentration-response relations of 1PBC at voltages from -140 to 140 mV, ΔV = 20 mV. Data are

512 calculated from (b), errors are SEM. Solid lines are fits to the Hill equation. **d**, IC₅₀ values obtained from

513 (c) at the indicated voltages. Data are best-fit values, errors are 95% CI. **e**, **f**, Concentration-response

514 relations of 1PBC of mouse TMEM16B (e) and TMEM16F (f) at 15 μM and 300 μM intracellular Ca²⁺

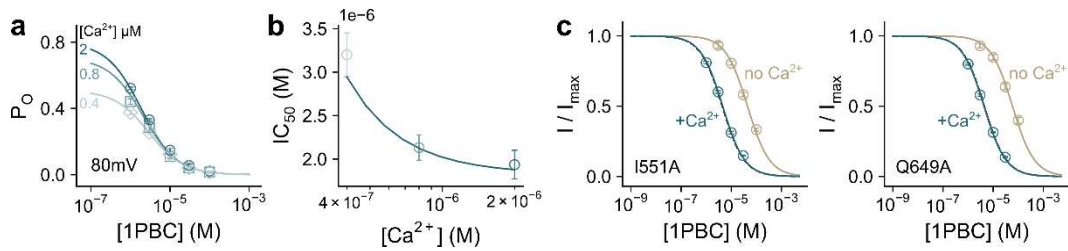
515 respectively at -80 and 80 mV. Data are averages of 5 and 6 biological replicates respectively, errors are

516 SEM. Solid lines are fits to the Hill equation. Dashed lines are the relations of TMEM16A. **g**, Sequence

517 alignment of the outer pore region of mouse TMEM16A (UniProt ID: Q8BHY3), mouse TMEM16B

518 (UniProtID: Q8CFW1), and mouse TMEM16F (UniProt ID: Q6P9J9). Sequence identity between
 519 TMEM16A and B, 60.5%; between TMEM16A and F, 39.5%. A conserved glycine in $\alpha 3$ is highlighted
 520 in grey and other colors indicate the type of the residues interacting with the blocker (yellow,
 521 hydrophobic; green, polar; blue, basic) in TMEM16A.

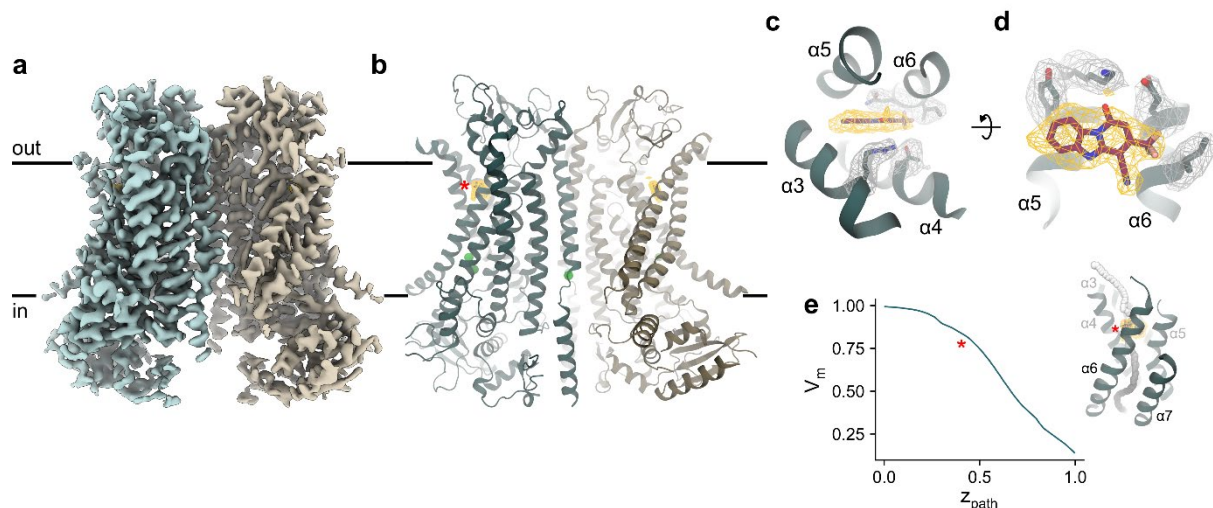
522



523

524 **Fig. 2: IPBC block is state-dependent. a**, Concentration-response relations of IPBC at the indicated
 525 intracellular Ca^{2+} concentrations at 80 mV. Data are scaled according to the open probability of the
 526 channel in the absence of IPBC as determined previously²⁸. Data are averages of 6, 5, and 7 biological
 527 replicates for 2 μ M, 800 nM, and 400 nM Ca^{2+} respectively, errors are SEM. **b**, IC_{50} values at the plotted
 528 intracellular Ca^{2+} concentrations at 80 mV, which were obtained via an empirical fit to the Hill equation
 529 on the data shown in (a). Shown are the best-fit values, errors are 95% CI. **a, b**, Solid lines are a global
 530 fit to an open-channel block mechanism (Eqs. 4-9), with estimated parameters $K_{d \text{ 1PBC}} = 3.6 \pm 0.29 \mu$ M
 531 at zero mV and apparent valence $\delta_b = 0.27 \pm 0.025$ (see 'Methods'). **c**, Concentration-response relations
 532 of IPBC at 0 mV at zero and 2 μ M intracellular Ca^{2+} for the constitutively active mutants I551A and
 533 Q649A. Data are averages of 6, 9, 7, and 7 biological replicates for I551A at 2 μ M Ca^{2+} , I551A at 0
 534 Ca^{2+} , Q649A at 2 μ M Ca^{2+} , and Q649A at 0 Ca^{2+} respectively, errors are SEM. Solid lines are fits to the
 535 Hill equation. Dashed lines are the relation of WT.

536



537

538 **Fig. 3: Structure of TMEM16A in complex with 1PBC and Ca²⁺.** **a, b,** Cryo-EM map (**a**) and ribbon

539 representation (**b**) of mouse TMEM16A in a 1PBC- and Ca²⁺-bound form viewed from within the

540 membrane. Black lines, membrane boundaries; green spheres, bound Ca²⁺; yellow mesh, density of the

541 bound 1PBC molecule. **c, d,** Close-up view of the binding site from the extracellular side (**c**) and from

542 within the membrane (**d**). Selected densities and sidechains are shown. **e,** Membrane potential profile of

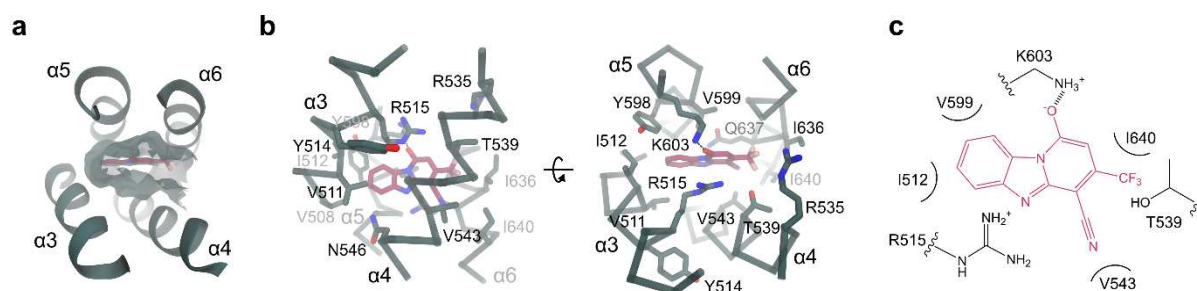
543 the pore in the 1PBC/Ca²⁺-bound structure. Inset, coordinates (spheres) where the transmembrane

544 potential was calculated. The spheres are colored according to the calculated values. The membrane

545 potential profile was calculated using the PBEQ module in CHARMM (see Methods). **b, e,** Asterisk

546 indicates the location of the 1PBC binding site.

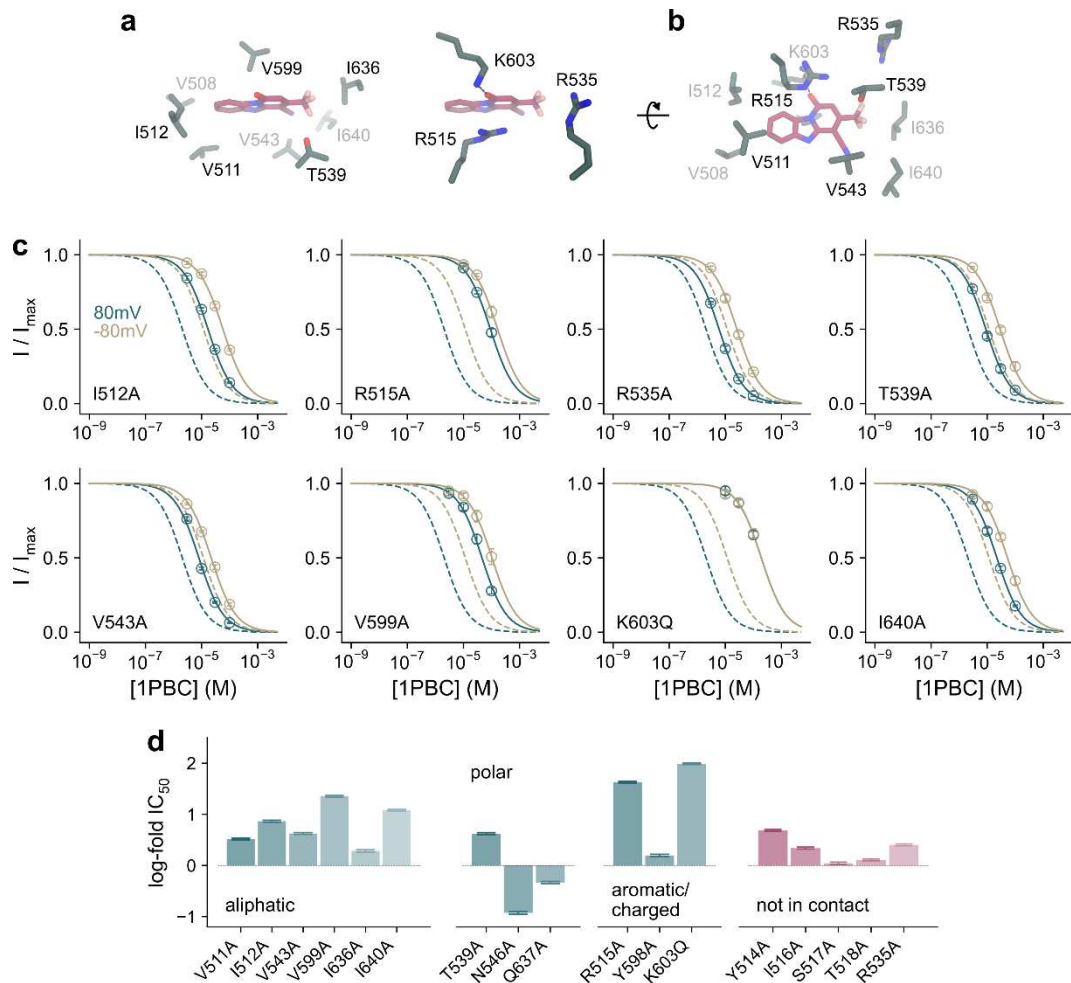
547



548

549 **Fig. 4: 1PBC binding site.** **a**, Position of 1PBC in the binding pocket viewed from the extracellular
 550 side. Molecular boundaries are represented as green surface. **b**, Detailed view of residues in contact
 551 distance to 1PBC. A putative salt bridge between Lys 603 and the 1PBC hydroxyl is indicated. **c**,
 552 Schematic contact map between 1PBC and selected surrounding residues.

553

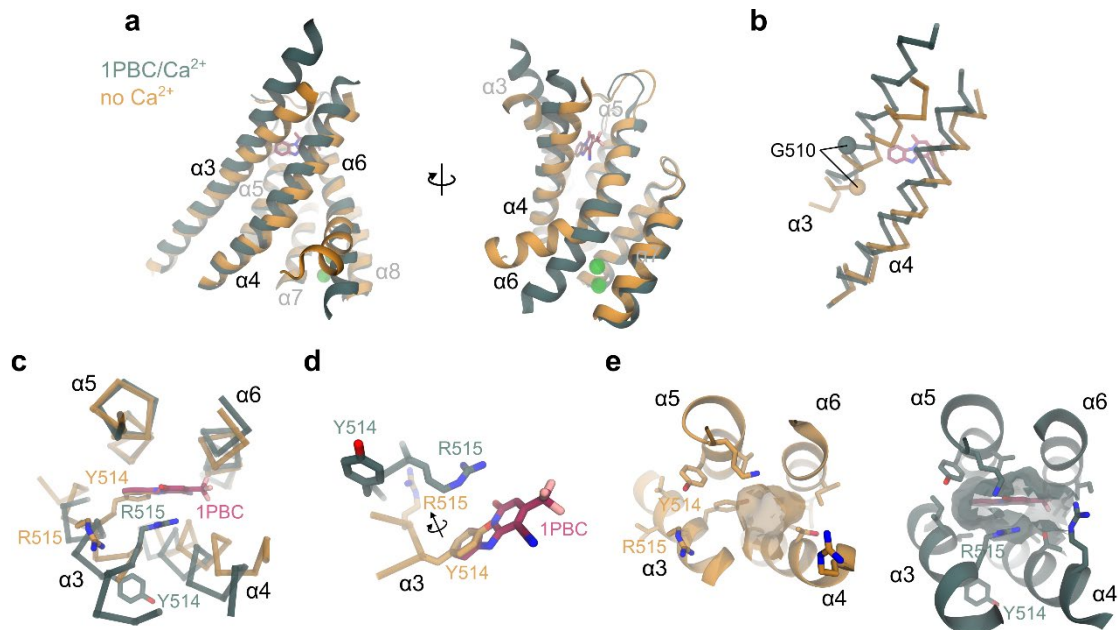


554

555 **Fig. 5: Interacting residues.** **a**, **b**, Close-up of selected residues surrounding the bound 1PBC. **c**,
 556 Concentration-response relations of 1PBC of selected mutants at a saturating Ca²⁺ concentration at -80
 557 and 80 mV. Data are averages of the indicated number of biological replicates shown in Supplementary
 558 Table 1, errors are SEM. Solid lines are fits to the Hill equation. Dashed lines are the relations of WT.
 559 **d**, Log-fold changes in IC₅₀ of mutants at 80 mV. Mutants of residues in contact with the blocker are

560 shown in green. Data are obtained via a fit to the Hill equation (Supplementary Figs. 6, 7), errors are
561 95% CI.

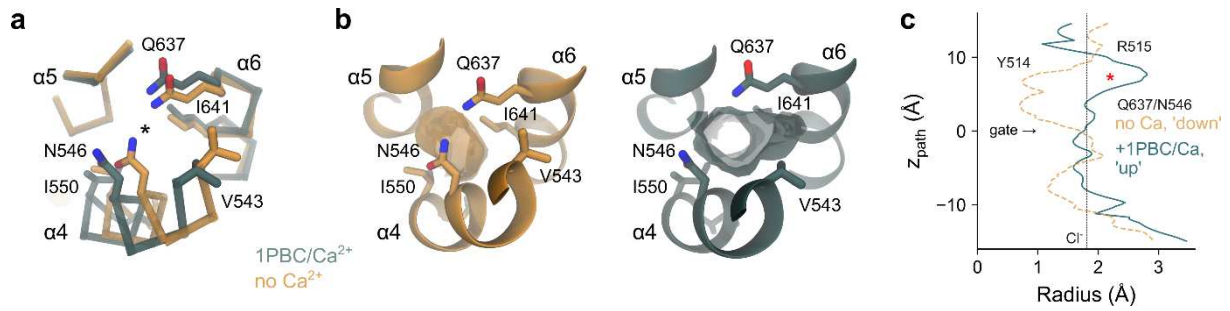
562



563

564 **Fig. 6: Rearrangement of the extracellular vestibule. a**, Superposition of the pore region of the rebuilt
565 Ca^{2+} -free apo (PDB: 5OYG) and the 1PBC/ Ca^{2+} -bound structures viewed from within the membrane.
566 **b**, $\alpha 3$ and $\alpha 4$ of the superposed structures in $\text{C}\alpha$ representation. The $\text{C}\alpha$ atoms of Gly 510 are shown as
567 spheres. **c**, $\alpha 3$ and $\alpha 4$ with respect to the other pore-forming helices in the superposed structures viewed
568 from the extracellular side. Selected residues on $\alpha 3$ are displayed. **d**, Close-up view of the residues that
569 rearrange upon the binding of 1PBC. **e**, Molecular surface of the extracellular vestibule viewed from the
570 top of the membrane. Selected residues lining the volume are shown. **a-e**, The 1PBC/ Ca^{2+} structure is
571 shown in green and the Ca^{2+} -free apo structure in gold.

572



573

574 **Fig. 7: Pore conformation. a**, Superposition of the narrow neck region of the hourglass-shaped pore of

575 the rebuilt Ca^{2+} -free apo (PDB: 5OYG) and the 1PBC/ Ca^{2+} -bound structures viewed from the top.

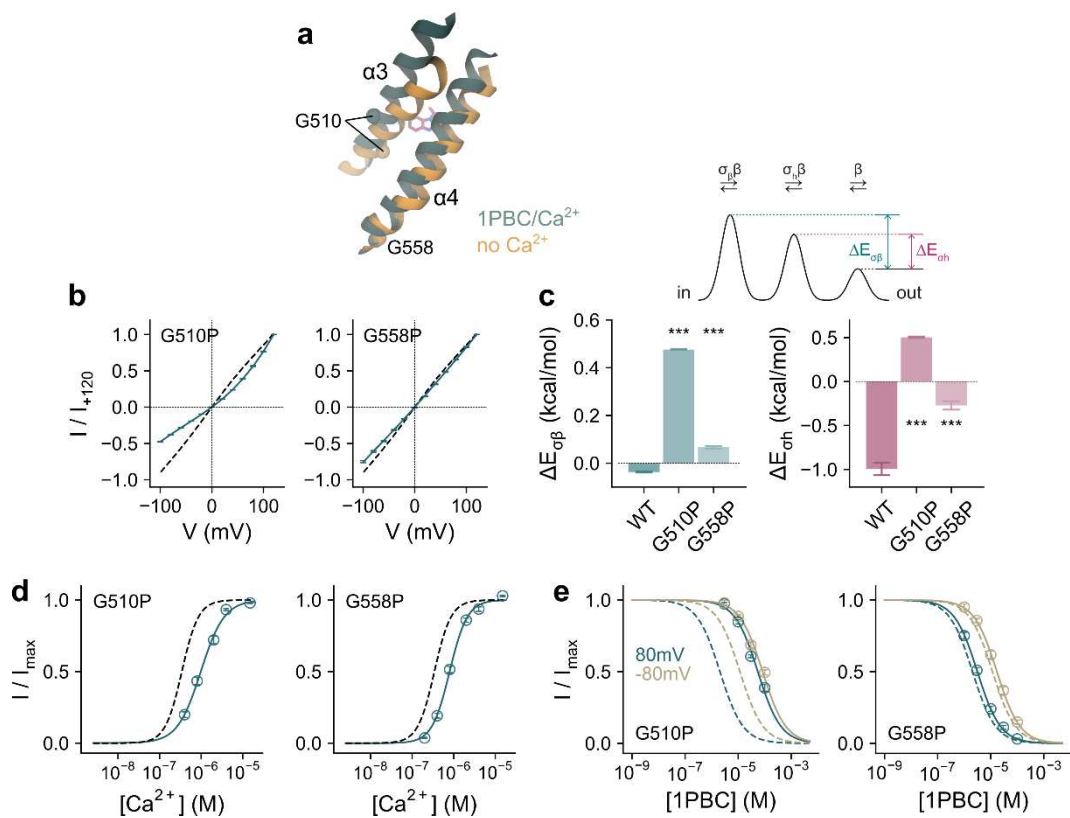
576 Asterisk indicates the pore axis. **b**, Molecular surface of the neck region viewed from the top. Selected

577 residues lining the volume are shown. **c**, Pore radius along the z-axis relative to the position of Ile 641

578 (gate). The locations of constrictions are indicated. Asterisk indicates the location of the 1PBC binding

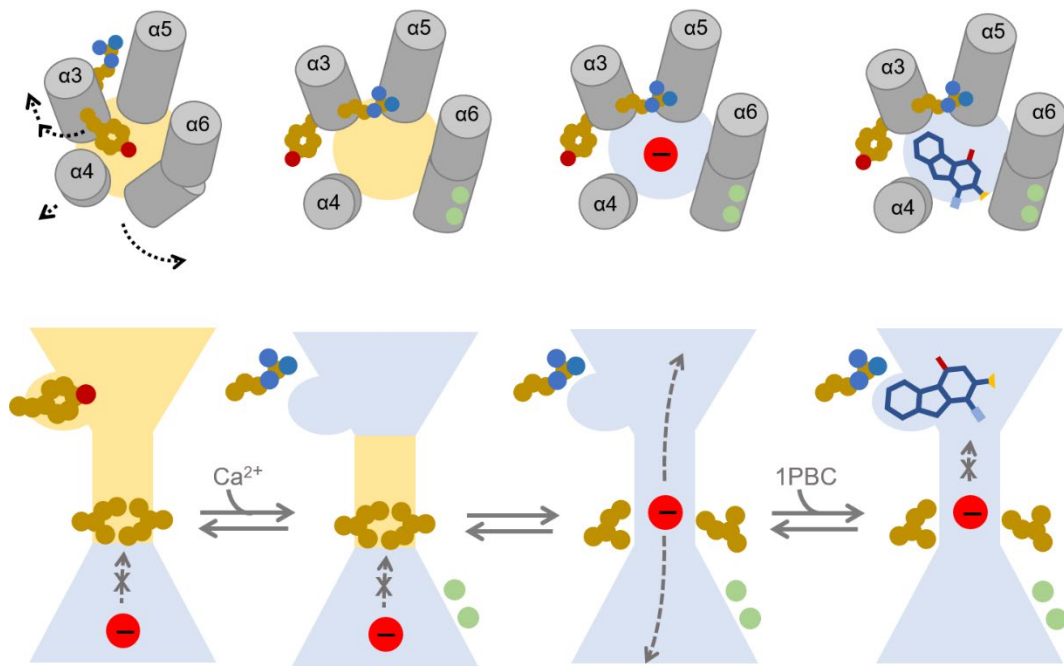
579 site. Dashed line denotes the ionic radius of a Cl^- ion.

580



581

582 **Fig. 8: Functional characterization of conformational changes.** **a**, Section of the pore in the
583 superposed 1PBC/Ca²⁺-bound and the rebuilt Ca²⁺-free apo structures viewed from within the
584 membrane. Spheres, C α of Gly 510 and Gly 558 on α 3 and α 4 respectively. **b**, Instantaneous current-
585 voltage relations of the indicated mutants at a saturating Ca²⁺ concentration (15 μ M and 50 μ M
586 respectively). Data are averages of 5 and 6 biological replicates for G510P and G558P respectively,
587 errors are SEM. Solid lines are fits to a model of ion permeation as described previously (Eq. 2)²³.
588 Dashed line is the relation of WT. **c**, Energy barrier relative to the outermost barrier in the ion conduction
589 path at the inner pore and the narrow neck region for the indicated mutants (Eq. 3 and see ‘Methods’).
590 Data are best-fit values obtained via the fits shown in (**b**), errors are 95% CI. Inset, minimal ion
591 permeation model illustrating the quantities plotted in (**c**). **d**, Ca²⁺ concentration-response relation of the
592 indicated mutants at 80 mV. Data are averages of 7 and 7 biological replicates for G510P and G558P
593 respectively, errors are SEM. Solid lines are fits to the Hill equation. Dashed lines are the relations of
594 WT. **e**, Concentration-response relations of 1PBC of the indicated mutants at a saturating Ca²⁺
595 concentration (15 μ M) at -80 and 80 mV. Data are averages of 9 and 8 biological replicates for G510P
596 and G558P respectively, errors are SEM. Solid lines are fits to the Hill equation. Dashed lines are the
597 relations of WT.



598

599 **Fig. 9: Mechanism.** In the Ca^{2+} -free closed state, constriction in both the narrow neck and extracellular
600 vestibule limits the access of either anions or the blocker 1PBC, whose binding site is occupied by Tyr
601 514 on $\alpha 3$. Ca^{2+} binding results in a series of transitions in the channel that opens the pore by rearranging
602 the outer vestibule. The outward movement of $\alpha 4$ widens the outer pore entrance, while the more
603 extended conformational change of $\alpha 3$ relocates Tyr 514 away from and projects the adjacent Arg 515
604 towards the pore lumen, creating a site that accommodates the blocker. These rearrangements are
605 subsequently propagated to the intracellular part of the narrow neck region to release a hydrophobic gate
606 that stabilizes the constricted pore in the closed state. The binding of the blocker to the site immediately
607 external to the narrow neck results in a direct blockade of the ion conduction path, thereby inhibiting
608 channel activity. Blocker access to a pre-open conformation, where the site is already remodeled but the
609 gate is still closed, appears to be feasible and might be represented in the observed structure.

610

611 **Table 1: Cryo-EM data collection, processing, refinement, and validation statistics**

	TMEM16A GDN Ca²⁺/1PBC Non-coated grids	TMEM16A GDN Ca²⁺/1PBC GO-coated grids
Data collection and processing		
Microscope	FEI Titan Krios G3i	FEI Titan Krios G3i
Camera	Gatan K3 GIF	Gatan K3 GIF
Imaging mode	Super-resolution counted	Super-resolution counted
Magnification	130,000	130,000
Voltage (kV)	300	300
Energy filter slit width (eV)	20	20
Electron dose (e ⁻ /Å ²)	61	70
Defocus range (μm)	-2.4 to -0.8	-2.4 to -0.8
Pixel size (Å) ^a	0.651 (0.326)	0.651 (0.326)
Initial particle images (no.)	2,203,806	1,596,293
Final particle images (no.)	13,897	87,916
Symmetry imposed	C2	
Map resolution (Å)	2.85	
FSC threshold 0.143		
Map resolution range (Å)	2.6-3.6	
Refinement		
Initial model	PDB: 7B5C	
Model resolution (Å)	2.92	
FSC threshold 0.5		
Map sharpening B factor (Å ²)	-82.7	
Model composition		
Non-hydrogen atoms	12,116	
Protein residues	1,472	
Ligands	1PBC: 2, Ca ²⁺ : 6	
B factors (Å ²)		
Protein	34.8	
Ligand	27.9	
r.m.s. deviations		
Bond lengths (Å)	0.002	
Bond angles (°)	0.511	
Validation		
MolProbity score	2.04	
Clash score	14.0	
Poor rotamers (%)	1.23	
Ramachandran plot		
Favored (%)	95.45	
Allowed (%)	4.41	
Disallowed (%)	0.14	

612 ^aValues in parentheses indicate the pixel size in super-resolution.

613

614 **References**

615

- 616 1 Caputo, A. *et al.* TMEM16A, a membrane protein associated with calcium-dependent chloride
617 channel activity. *Science* **322**, 590-594, doi:10.1126/science.1163518 (2008).
- 618 2 Schroeder, B. C., Cheng, T., Jan, Y. N. & Jan, L. Y. Expression cloning of TMEM16A as a
619 calcium-activated chloride channel subunit. *Cell* **134**, 1019-1029,
620 doi:10.1016/j.cell.2008.09.003 (2008).
- 621 3 Yang, Y. D. *et al.* TMEM16A confers receptor-activated calcium-dependent chloride
622 conductance. *Nature* **455**, 1210-1215, doi:10.1038/nature07313 (2008).
- 623 4 Suzuki, J., Umeda, M., Sims, P. J. & Nagata, S. Calcium-dependent phospholipid scrambling
624 by TMEM16F. *Nature* **468**, 834-838, doi:10.1038/nature09583 (2010).
- 625 5 Yang, H. *et al.* TMEM16F forms a Ca²⁺-activated cation channel required for lipid scrambling
626 in platelets during blood coagulation. *Cell* **151**, 111-122, doi:10.1016/j.cell.2012.07.036 (2012).
- 627 6 Malvezzi, M. *et al.* Ca²⁺-dependent phospholipid scrambling by a reconstituted TMEM16 ion
628 channel. *Nat Commun* **4**, 2367, doi:10.1038/ncomms3367 (2013).
- 629 7 Suzuki, J. *et al.* Calcium-dependent phospholipid scramblase activity of TMEM16 protein
630 family members. *J Biol Chem* **288**, 13305-13316, doi:10.1074/jbc.M113.457937 (2013).
- 631 8 Brunner, J. D., Lim, N. K., Schenck, S., Duerst, A. & Dutzler, R. X-ray structure of a calcium-
632 activated TMEM16 lipid scramblase. *Nature* **516**, 207-212, doi:10.1038/nature13984 (2014).
- 633 9 Hartzell, C., Putzier, I. & Arreola, J. Calcium-activated chloride channels. *Annu Rev Physiol* **67**,
634 719-758, doi:10.1146/annurev.physiol.67.032003.154341 (2005).
- 635 10 Pedemonte, N. & Galiotta, L. J. Structure and function of TMEM16 proteins (anoctamins).
636 *Physiol Rev* **94**, 419-459, doi:10.1152/physrev.00039.2011 (2014).
- 637 11 Oh, U. & Jung, J. Cellular functions of TMEM16/anoctamin. *Pflugers Arch* **468**, 443-453,
638 doi:10.1007/s00424-016-1790-0 (2016).
- 639 12 Falzone, M. E., Malvezzi, M., Lee, B. C. & Accardi, A. Known structures and unknown
640 mechanisms of TMEM16 scramblases and channels. *J Gen Physiol* **150**, 933-947,
641 doi:10.1085/jgp.201711957 (2018).
- 642 13 Huang, F. *et al.* Calcium-activated chloride channel TMEM16A modulates mucin secretion and
643 airway smooth muscle contraction. *Proc Natl Acad Sci U S A* **109**, 16354-16359,
644 doi:10.1073/pnas.1214596109 (2012).
- 645 14 Heinze, C. *et al.* Disruption of vascular Ca²⁺-activated chloride currents lowers blood pressure.
646 *J Clin Invest* **124**, 675-686, doi:10.1172/JCI70025 (2014).

- 647 15 Li, H., Salomon, J. J., Sheppard, D. N., Mall, M. A. & Galiotta, L. J. Bypassing CFTR
648 dysfunction in cystic fibrosis with alternative pathways for anion transport. *Curr Opin*
649 *Pharmacol* **34**, 91-97, doi:10.1016/j.coph.2017.10.002 (2017).
- 650 16 Kunzelmann, K. *et al.* TMEM16A in Cystic Fibrosis: Activating or Inhibiting? *Front*
651 *Pharmacol* **10**, 3, doi:10.3389/fphar.2019.00003 (2019).
- 652 17 Quesada, R. & Dutzler, R. Alternative chloride transport pathways as pharmacological targets
653 for the treatment of cystic fibrosis. *J Cyst Fibros* **19**, S37-S41, doi:10.1016/j.jcf.2019.10.020
654 (2020).
- 655 18 Danahay, H. & Gosling, M. TMEM16A: An Alternative Approach to Restoring Airway Anion
656 Secretion in Cystic Fibrosis? *Int J Mol Sci* **21**, doi:10.3390/ijms21072386 (2020).
- 657 19 Braga, L. *et al.* Drugs that inhibit TMEM16 proteins block SARS-CoV-2 spike-induced
658 syncytia. *Nature* **594**, 88-93, doi:10.1038/s41586-021-03491-6 (2021).
- 659 20 Jeng, G., Aggarwal, M., Yu, W. P. & Chen, T. Y. Independent activation of distinct pores in
660 dimeric TMEM16A channels. *J Gen Physiol* **148**, 393-404, doi:10.1085/jgp.201611651 (2016).
- 661 21 Lim, N. K., Lam, A. K. & Dutzler, R. Independent activation of ion conduction pores in the
662 double-barreled calcium-activated chloride channel TMEM16A. *J Gen Physiol* **148**, 375-392,
663 doi:10.1085/jgp.201611650 (2016).
- 664 22 Paulino, C., Kalienkova, V., Lam, A. K. M., Neldner, Y. & Dutzler, R. Activation mechanism
665 of the calcium-activated chloride channel TMEM16A revealed by cryo-EM. *Nature* **552**, 421-
666 425, doi:10.1038/nature24652 (2017).
- 667 23 Paulino, C. *et al.* Structural basis for anion conduction in the calcium-activated chloride channel
668 TMEM16A. *Elife* **6** (2017).
- 669 24 Dang, S. *et al.* Cryo-EM structures of the TMEM16A calcium-activated chloride channel.
670 *Nature* **552**, 426-429, doi:10.1038/nature25024 (2017).
- 671 25 Lam, A. K. & Dutzler, R. Calcium-dependent electrostatic control of anion access to the pore
672 of the calcium-activated chloride channel TMEM16A. *Elife* **7**, doi:10.7554/eLife.39122 (2018).
- 673 26 Xiao, Q. *et al.* Voltage- and calcium-dependent gating of TMEM16A/Ano1 chloride channels
674 are physically coupled by the first intracellular loop. *Proc Natl Acad Sci U S A* **108**, 8891-8896,
675 doi:10.1073/pnas.1102147108 (2011).
- 676 27 Lam, A. K. M., Rheinberger, J., Paulino, C. & Dutzler, R. Gating the pore of the calcium-
677 activated chloride channel TMEM16A. *Nat Commun* **12**, 785, doi:10.1038/s41467-020-20787-
678 9 (2021).
- 679 28 Lam, A. K. M. & Dutzler, R. Mechanism of pore opening in the calcium-activated chloride
680 channel TMEM16A. *Nat Commun* **12**, 786, doi:10.1038/s41467-020-20788-8 (2021).
- 681 29 Le, S. C. & Yang, H. An Additional Ca(2+) Binding Site Allosterically Controls TMEM16A
682 Activation. *Cell Rep* **33**, 108570, doi:10.1016/j.celrep.2020.108570 (2020).

- 683 30 Bushell, S. R. *et al.* The structural basis of lipid scrambling and inactivation in the endoplasmic
684 reticulum scramblase TMEM16K. *Nat Commun* **10**, 3956, doi:10.1038/s41467-019-11753-1
685 (2019).
- 686 31 Alvadia, C. *et al.* Cryo-EM structures and functional characterization of the murine lipid
687 scramblase TMEM16F. *Elife* **8**, doi:10.7554/eLife.44365 (2019).
- 688 32 Jia, Z. & Chen, J. Specific PIP2 binding promotes calcium activation of TMEM16A chloride
689 channels. *Commun Biol* **4**, 259, doi:10.1038/s42003-021-01782-2 (2021).
- 690 33 Le, S. C., Jia, Z., Chen, J. & Yang, H. Molecular basis of PIP2-dependent regulation of the
691 Ca(2+)-activated chloride channel TMEM16A. *Nat Commun* **10**, 3769, doi:10.1038/s41467-
692 019-11784-8 (2019).
- 693 34 Ta, C. M., Acheson, K. E., Rorsman, N. J. G., Jongkind, R. C. & Tammaro, P. Contrasting
694 effects of phosphatidylinositol 4,5-bisphosphate on cloned TMEM16A and TMEM16B
695 channels. *Br J Pharmacol* **174**, 2984-2999, doi:10.1111/bph.13913 (2017).
- 696 35 Tembo, M., Wozniak, K. L., Bainbridge, R. E. & Carlson, A. E. Phosphatidylinositol 4,5-
697 bisphosphate (PIP2) and Ca(2+) are both required to open the Cl(-) channel TMEM16A. *J Biol*
698 *Chem* **294**, 12556-12564, doi:10.1074/jbc.RA118.007128 (2019).
- 699 36 Ye, W. *et al.* Phosphatidylinositol-(4, 5)-bisphosphate regulates calcium gating of small-
700 conductance cation channel TMEM16F. *Proc Natl Acad Sci U S A* **115**, E1667-E1674,
701 doi:10.1073/pnas.1718728115 (2018).
- 702 37 Yu, K., Jiang, T., Cui, Y., Tajkhorshid, E. & Hartzell, H. C. A network of phosphatidylinositol
703 4,5-bisphosphate binding sites regulates gating of the Ca(2+)-activated Cl(-) channel ANO1
704 (TMEM16A). *Proc Natl Acad Sci U S A* **116**, 19952-19962, doi:10.1073/pnas.1904012116
705 (2019).
- 706 38 Namkung, W., Yao, Z., Finkbeiner, W. E. & Verkman, A. S. Small-molecule activators of
707 TMEM16A, a calcium-activated chloride channel, stimulate epithelial chloride secretion and
708 intestinal contraction. *FASEB J* **25**, 4048-4062, doi:10.1096/fj.11-191627 (2011).
- 709 39 De La Fuente, R., Namkung, W., Mills, A. & Verkman, A. S. Small-molecule screen identifies
710 inhibitors of a human intestinal calcium-activated chloride channel. *Mol Pharmacol* **73**, 758-
711 768, doi:10.1124/mol.107.043208 (2008).
- 712 40 Namkung, W., Phuan, P. W. & Verkman, A. S. TMEM16A inhibitors reveal TMEM16A as a
713 minor component of calcium-activated chloride channel conductance in airway and intestinal
714 epithelial cells. *J Biol Chem* **286**, 2365-2374, doi:10.1074/jbc.M110.175109 (2011).
- 715 41 Oh, S. J. *et al.* MONNA, a potent and selective blocker for transmembrane protein with
716 unknown function 16/anoctamin-1. *Mol Pharmacol* **84**, 726-735, doi:10.1124/mol.113.087502
717 (2013).
- 718 42 Seo, Y. *et al.* Ani9, A Novel Potent Small-Molecule ANO1 Inhibitor with Negligible Effect on
719 ANO2. *PLoS One* **11**, e0155771, doi:10.1371/journal.pone.0155771 (2016).

- 720 43 Danahay, H. L. *et al.* TMEM16A Potentiation: A Novel Therapeutic Approach for the
721 Treatment of Cystic Fibrosis. *Am J Resp Crit Care* **201**, 946-954, doi:10.1164/rccm.201908-
722 1641OC (2020).
- 723 44 Peters, C. J. *et al.* Four basic residues critical for the ion selectivity and pore blocker sensitivity
724 of TMEM16A calcium-activated chloride channels. *Proc Natl Acad Sci U S A* **112**, 3547-3552,
725 doi:10.1073/pnas.1502291112 (2015).
- 726 45 Genovese, M. *et al.* TRPV4 and purinergic receptor signalling pathways are separately linked
727 in airway epithelia to CFTR and TMEM16A chloride channels. *J Physiol* **597**, 5859-5878,
728 doi:10.1113/JP278784 (2019).
- 729 46 Boedtker, D. M., Kim, S., Jensen, A. B., Matchkov, V. M. & Andersson, K. E. New selective
730 inhibitors of calcium-activated chloride channels - T16A(inh) -A01, CaCC(inh) -A01 and
731 MONNA - what do they inhibit? *Br J Pharmacol* **172**, 4158-4172, doi:10.1111/bph.13201
732 (2015).
- 733 47 Shi, S. *et al.* Molecular mechanism of CaCCinh-A01 inhibiting TMEM16A channel. *Arch*
734 *Biochem Biophys* **695**, 108650, doi:10.1016/j.abb.2020.108650 (2020).
- 735 48 Shi, S., Ma, B., Sun, F., Qu, C. & An, H. Theaflavin binds to a druggable pocket of TMEM16A
736 channel and inhibits lung adenocarcinoma cell viability. *J Biol Chem* **297**, 101016,
737 doi:10.1016/j.jbc.2021.101016 (2021).
- 738 49 Qu, Z. & Hartzell, H. C. Functional geometry of the permeation pathway of Ca²⁺-activated Cl-
739 channels inferred from analysis of voltage-dependent block. *J Biol Chem* **276**, 18423-18429,
740 doi:10.1074/jbc.M101264200 (2001).
- 741 50 Ta, C. M., Adomaviciene, A., Rorsman, N. J., Garnett, H. & Tammaro, P. Mechanism of
742 allosteric activation of TMEM16A/ANO1 channels by a commonly used chloride channel
743 blocker. *Br J Pharmacol* **173**, 511-528, doi:10.1111/bph.13381 (2016).
- 744 51 Miner, K. *et al.* Drug Repurposing: The Anthelmintics Niclosamide and Nitazoxanide Are
745 Potent TMEM16A Antagonists That Fully Bronchodilate Airways. *Front Pharmacol* **10**, 51,
746 doi:10.3389/fphar.2019.00051 (2019).
- 747 52 Dixon, S. L. & Jurs, P. C. Estimation of pKa for organic oxyacids using calculated atomic
748 charges. *Journal of computational chemistry* **14**, 1460-1467,
749 doi:<https://doi.org/10.1002/jcc.540141208> (1993).
- 750 53 Peters, C. J. *et al.* The Sixth Transmembrane Segment Is a Major Gating Component of the
751 TMEM16A Calcium-Activated Chloride Channel. *Neuron* **97**, 1063-+,
752 doi:10.1016/j.neuron.2018.01.048 (2018).
- 753 54 Dinsdale, R. L. *et al.* An outer-pore gate modulates the pharmacology of the TMEM16A
754 channel. *Proc Natl Acad Sci U S A* **118**, doi:10.1073/pnas.2023572118 (2021).
- 755 55 Jiang, Y. *et al.* The open pore conformation of potassium channels. *Nature* **417**, 523-526,
756 doi:10.1038/417523a (2002).

- 757 56 Falzone, M. E. *et al.* Structural basis of Ca(2+)-dependent activation and lipid transport by a
758 TMEM16 scramblase. *Elife* **8**, doi:10.7554/eLife.43229 (2019).
- 759 57 Kalienkova, V. *et al.* Stepwise activation mechanism of the scramblase nhTMEM16 revealed
760 by cryo-EM. *Elife* **8**, doi:10.7554/eLife.44364 (2019).
- 761 58 Zheng, L., Baumann, U. & Reymond, J. L. An efficient one-step site-directed and site-saturation
762 mutagenesis protocol. *Nucleic Acids Res* **32**, e115, doi:10.1093/nar/gnh110 (2004).
- 763 59 Palovcak, E. *et al.* A simple and robust procedure for preparing graphene-oxide cryo-EM grids.
764 *J Struct Biol* **204**, 80-84, doi:10.1016/j.jsb.2018.07.007 (2018).
- 765 60 Zivanov, J. *et al.* New tools for automated high-resolution cryo-EM structure determination in
766 RELION-3. *Elife* **7**, doi:10.7554/eLife.42166 (2018).
- 767 61 Zheng, S. Q. *et al.* MotionCor2: anisotropic correction of beam-induced motion for improved
768 cryo-electron microscopy. *Nat Methods* **14**, 331-332, doi:10.1038/nmeth.4193 (2017).
- 769 62 Zhang, K. Gctf: Real-time CTF determination and correction. *J Struct Biol* **193**, 1-12,
770 doi:10.1016/j.jsb.2015.11.003 (2016).
- 771 63 Wagner, T. *et al.* SPHIRE-crYOLO is a fast and accurate fully automated particle picker for
772 cryo-EM. *Commun Biol* **2**, 218, doi:10.1038/s42003-019-0437-z (2019).
- 773 64 Tan, Y. Z. *et al.* Addressing preferred specimen orientation in single-particle cryo-EM through
774 tilting. *Nature Methods* **14**, 793-+, doi:10.1038/Nmeth.4347 (2017).
- 775 65 Pettersen, E. F. *et al.* UCSF Chimera--a visualization system for exploratory research and
776 analysis. *Journal of computational chemistry* **25**, 1605-1612, doi:10.1002/jcc.20084 (2004).
- 777 66 Moriarty, N. W., Grosse-Kunstleve, R. W. & Adams, P. D. electronic Ligand Builder and
778 Optimization Workbench (eLBOW): a tool for ligand coordinate and restraint generation. *Acta*
779 *Crystallogr D Biol Crystallogr* **65**, 1074-1080, doi:10.1107/S0907444909029436 (2009).
- 780 67 Emsley, P. & Cowtan, K. Coot: model-building tools for molecular graphics. *Acta Crystallogr*
781 *D Biol Crystallogr* **60**, 2126-2132, doi:S0907444904019158 [pii]
782 10.1107/S0907444904019158 (2004).
- 783 68 Adams, P. D. *et al.* PHENIX: building new software for automated crystallographic structure
784 determination. *Acta Crystallogr D Biol Crystallogr* **58**, 1948-1954 (2002).
- 785 69 Davis, I. W., Murray, L. W., Richardson, J. S. & Richardson, D. C. MOLPROBITY: structure
786 validation and all-atom contact analysis for nucleic acids and their complexes. *Nucleic Acids*
787 *Res* **32**, W615-619, doi:10.1093/nar/gkh398 (2004).
- 788 70 Smart, O. S., Neduvelil, J. G., Wang, X., Wallace, B. A. & Sansom, M. S. HOLE: a program
789 for the analysis of the pore dimensions of ion channel structural models. *Journal of molecular*
790 *graphics* **14**, 354-360, 376 (1996).

- 791 71 Humphrey, W., Dalke, A. & Schulten, K. VMD: visual molecular dynamics. *Journal of*
792 *molecular graphics* **14**, 33-38, 27-38, doi:10.1016/0263-7855(96)00018-5 (1996).
- 793 72 Goddard, T. D. *et al.* UCSF ChimeraX: Meeting modern challenges in visualization and
794 analysis. *Protein Sci* **27**, 14-25, doi:10.1002/pro.3235 (2018).
- 795 73 Colquhoun, D. & Hawkes, A. G. in *Single-Channel Recording* (eds B. Sakmann & E. Neher)
796 Ch. 20, 589-633 (Kluwer Academic/Plenum Publishers, 1995).
- 797 74 Colquhoun, D. & Hawkes, A. G. Relaxation and fluctuations of membrane currents that flow
798 through drug-operated channels. *Proc R Soc Lond B Biol Sci* **199**, 231-262,
799 doi:10.1098/rspb.1977.0137 (1977).
- 800 75 Roux, B. Influence of the membrane potential on the free energy of an intrinsic protein. *Biophys*
801 *J* **73**, 2980-2989, doi:10.1016/S0006-3495(97)78327-9 (1997).
- 802 76 Im, W., Beglov, D. & Roux, B. Continuum Solvation Model: computation of electrostatic forces
803 from numerical solutions to the Poisson-Boltzmann equation. *Comput Phys Commun* **111**, 59-
804 75, doi:Doi 10.1016/S0010-4655(98)00016-2 (1998).
- 805 77 Brooks, B. R. *et al.* Charmm - a Program for Macromolecular Energy, Minimization, and
806 Dynamics Calculations. *Journal of computational chemistry* **4**, 187-217, doi:DOI
807 10.1002/jcc.540040211 (1983).
- 808

Supplementary Files

This is a list of supplementary files associated with this preprint. Click to download.

- [sourcedataRDutzlerrevision.zip](#)